SCIENCE CHINA
Information Sciences

• **Supplementary File** •

Orbitronics for energy-efficient magnetization switching

Yuxuan Yao[1#], Daoqian Zhu[1,2#*], Qingtao Xia[1,3#], Jianing Liang[4], Yuhao Jiang[1], Zhiyang Peng[1], Jiaxu Li[1], Chen Xiao[1], Renyou Xu[1], Wenwen Wang[4], Xiantao Shang[4], Shiyang Lu[1,3], Dapeng Zhu[1,3], Hong-Xi Liu[4], Kaihua Cao[1,3] & Weisheng Zhao[1,2,3*]

[1]*Fert Beijing Institute, School of Integrated Circuit Science and Engineering, Beihang University, Beijing* 100191*, China;*
[2]*National Key Lab of Spintronics, Institute of International Innovation, Beihang University, Hangzhou* 311115*, China;*
[3]*Qingdao Research Institute, Beihang University, Qingdao* 266000*, China;*
[4]*Truth Memory Corporation, Beijing* 100088*, China;*
[#]*These authors contributed equally to this work.*

Appendix A Experimental methods

Appendix A.1 Sample deposition and characterization

All samples were deposited by DC and RF magnetron sputtering on thermally oxidized Si substrates. The base pressure of the sputtering chamber is better than 7×10^{-8} Torr. After deposition, all the samples were annealed at 300°C for 20 minutes with an in-plane magnetic field of 1 T if not specially stated. A vibrating sample magnetometer (VSM) was used to perform the measurements of magnetic properties of all the samples. The resistivity of each layer was determined by the four-probe method after annealing, see supporting table A1. X-ray diffraction (XRD) measurements were performed by a Bruker JV Delta-X X-ray metrology system with Cu Kα radiation. The generator voltage and current were set to be 40 kV and 40 mA, respectively.

Appendix A.2 Device fabrication and Electrical measurements

After annealing, samples were patterned into Hall-bar devices with a width of 10 μm by ultraviolet (UV) photolithography and ion-beam etching (IBE). Four electrodes of Ti(50)/AlCu(150)/TiN(10) for each Hall-bar device were deposited and patterned by magnetron sputtering and lift-off process.

Second harmonic Hall voltage measurements were performed with an AC current source and two lock-in amplifiers. The frequency of the applied AC current was 133.33 Hz. Current-induced magnetization switching measurements were performed by current pulses applied along the x-axis by the current source, and Hall voltages were measured along the y-axis by a nanovoltmeter, as shown in Figure 1(b). The Hall voltage were measured after each switching current pulse with a reading current pulse of 1 mA.

Appendix A.3 Thickness dependent resistivity of Ta and other materials

Samples with two conditions of Ta were sputtered by changing the power supply, substrate-target distance, and working pressure. For condition 1, an extra sample of Ta(t)/MgO(1.5)/Ta(1) was deposited without rotating the substrate, forming a wedge structure. The resistivity of Ta was confirmed by four-probe method before and after annealing at 300°C for 20 minutes on this sample. As shown in Figure A1, the resistivity decreases with the thickness of Ta firstly and then reaches a plateau with a resistivity of ∼160 $\mu\Omega$·cm, indicating a robust β phase. For sputtering condition 2, the resistivity of Ta(8) is 130 $\mu\Omega$·cm, indicating a mixed phase. We can exclude the existence of α-Ta and compare the result of Ta with these two conditions. For other materials, e.g., Ru, W and Cr, we summarize their resistivities in Table A1.

Table A1 Resistivity of materials

Material	Thickness	Resistivity
Ta	8 nm	162 $\mu\Omega$·cm
α-W	8 nm	23 $\mu\Omega$·cm
Cr	8 nm	50 $\mu\Omega$·cm
Ru	8 nm	30 $\mu\Omega$·cm
Pt	2 nm	55 $\mu\Omega$·cm
Pt	10 nm	23 $\mu\Omega$·cm

* Corresponding author (email: daoqian_zhu@buaa.edu.cn, weisheng.zhao@buaa.edu.cn)

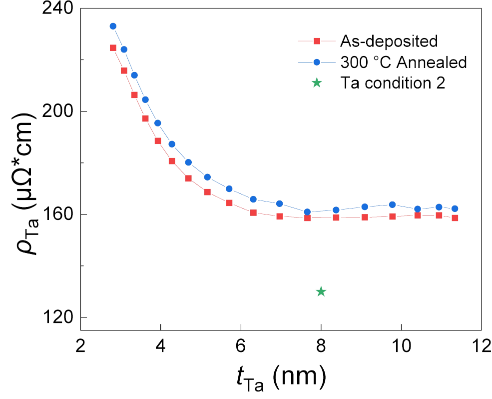

Figure A1 Resistivity of Ta with sputtering conditions 1 and 2. For condition 1, thickness dependent resistivities before and after annealing at 300 ℃ are shown by red squares and blue circles.

Appendix B Current-to-spin conversion efficiency of Ta/Pt bilayers

We first studied the charge-to-spin conversion efficiency in Ta/Pt/CoFeB/MgO multilayers. We prepared two series of stacks:

1. Ta($t_{\rm Ta}$)/Pt(2)/CoFeB(1.5)/MgO(1.5)/Ta(2),

2. Ta(8)/Pt($t_{\rm Pt}$)/CoFeB(1.5)/MgO(1.5)/Ta(2).

The MgO(1.5)/Ta(2) layers were capping layers to prevent oxidation for all the samples and will not be mentioned below. For each series, the orbital current source Ta layer was deposited using two sputtering conditions for different resistivity. When varying $t_{\rm Ta}$ from 6 nm to 12 nm, the resistivity of Ta was determined to be $\sim$160 $\mu\Omega$·cm or $\sim$130 $\mu\Omega$·cm (Figure A1) for conditions 1 and 2, respectively, excluding the existence of α-Ta.

We investigated the charge-to-spin conversion efficiency in Hall-bar devices, as shown in Figure 1(b). To quantify the $\theta_{\rm H}$ for the Ta/Pt bilayer, we performed second harmonic Hall voltage measurements in these Hall-bar devices. By sweeping azimuthal angle φ and magnitude of the applied external field, the measured second harmonic Hall resistance reads [1, 2]:

$$R_{\rm xy}^{2\omega}(\varphi) = \left(R_{\rm A}\frac{B_{\rm DL}}{2(B_{\rm ext}+\mu_0 M_{\rm eff})} - R_{\rm P}\frac{B_{\rm FL+Oe}}{2B_{\rm ext}} + R_{\nabla {\rm T}}\right)\cos\varphi - R_{\rm P}\frac{B_{\rm FL+Oe}}{2B_{\rm ext}}\cos 3\varphi, \tag{B1}$$

where $R_{\rm A}$ is anomalous Hall effect (AHE) resistance, $R_{\rm P}$ is planer Hall effect (PHE) resistance determined by first harmonic signal, $R_{\nabla {\rm T}}$ is thermal contributions, $B_{\rm DL}$ is the damping-like torque effective field, $B_{\rm FL+Oe}$ is the contributions from the field-like torque effective field and the Oersted field, $B_{\rm ext}$ is the applied external magnetic field, and $M_{\rm eff}$ is effective out-of-plane magnetic field, including demagnetizing field and interfacial perpendicular anisotropy field. Angular-dependent first and second harmonic Hall resistance $R_{\rm xy}^{1\omega}(\varphi)$ and $R_{\rm xy}^{2\omega}(\varphi)$ signals of Ta(8)/Pt(2)/CoFeB(1.5) are shown in Figures B1(a) and B1(b), respectively. By disentangling $\cos\varphi$ and $\cos 3\varphi$ contributions in the $R_{\rm xy}^{2\omega}(\varphi)$ signal, we can determine $B_{\rm DL}$ and $B_{\rm FL+Oe}$ by fitting $\cos\varphi - \cos 3\varphi$ signal magnitude and $\cos 3\varphi$ signal magnitude to $\frac{1}{B_{\rm ext}+\mu_0 M_{\rm eff}}$ and $\frac{1}{B_{\rm ext}}$, respectively, as shown in Figure B1(c). Thermal contributions can be excluded by these fittings. Note that the measured $B_{\rm FL+Oe}$ is negligible compared to $B_{\rm DL}$ and was not shown here. The $B_{\rm DL}$ can be determined by:

$$B_{\rm DL} = \frac{\hbar J_{\rm SOT}\theta_{\rm H}}{2eM_{\rm S}t_{\rm F}}, \tag{B2}$$

where $\hbar$ is the reduced Planck constant, e is the electron charge, $M_{\rm S}$ is the saturation magnetization of the sample, $t_{\rm F}$ is the thickness of the ferromagnetic layer, and $J_{\rm SOT}$ is the applied charge current density into Ta/Pt bilayer SOT channel.

Figures 1(b) and (c) summarize the measured $\theta_{\rm H}$ for these two series. In series 1 with the thickness of Pt fixed to 2 nm, the Ta thicknesses $t_{\rm Ta} = 0, 2, 6, 8, 10, 12$ nm were investigated. We can see that $\theta_{\rm H}$ of the Ta/Pt bilayer SOT channel increases with the thickness of Ta prepared at condition 1 (Figure 1(b)). We also changed the thickness of the CoFeB layer to 3 nm, resulting in nearly the same $\theta_{\rm H}$, as shown in Figure 1(b) with green triangle. Similar efficiency was obtained for samples deposited at condition 2 when $t_{\rm Ta} = 6, 8$ nm (for samples with Ta condition 2, the thickness of CoFeB is 3 nm).

Appendix C Comparison of different orbital sources

In addition to the Ta/Pt, we investigated other X/Pt bilayer as SOT channels (X = Cr, W, Ru) because all of them have been predicted to present strong OHC. Under the same deposition and annealing conditions as the Ta series, we prepared the X(8)/Pt(2)/CoFeB(1.5)/MgO(1.5)/Ta(2) samples. All the X/Pt bilayers possess a positive sign of $\theta_{\rm H}$, as illustrated by the second harmonic Hall voltage signals in Figure C1(a). Besides the difference of $\theta_{\rm H}$, due to the large difference of resistivities in these materials, we calculated the effective Hall conductivity $\sigma_{\rm H}^{\rm eff}$ of the Ta(10), Pt(10), X(8)/Pt(2) (X= Ta, Cr, W, Ru). As shown in Figure C1(b), the $\sigma_{\rm H}^{\rm eff}$ of the Ta(8)/Pt(2) bilayer is significantly larger than the Ta(10) monolayer and has the opposite sign. Comparing to other X(8)/Pt(2) bilayers, its $\sigma_{\rm H}^{\rm eff}$ is larger than Cr(8)/Pt(2) bilayer and similar to W(8)/Pt (2) bilayers. Ru(8)/Pt(2) bilayer possesses a larger $\sigma_{\rm H}^{\rm eff}$ thanks to its low resistivity, similar with that of Pt(10). The unexpected result may be due to larger orbital diffusion length $\lambda_{\rm OHE}$ in Cr [3], Ru ($\theta_{\rm H}$ of Ru(12)/Pt(2) reaches 0.1 and $\sigma_{\rm H}^{\rm eff}$ of Ru(12)/Pt(2) reaches $3.2\times10^5(\frac{\hbar}{e}\cdot\Omega^{-1}\cdot{\rm m}^{-1})$, larger than that of Pt(10), see cyan dot in Figures 1(d) and C1(b)) and W [4]. As such, the $\theta_{\rm H}$ in these bilayers may not be saturated when the thickness of X is only 8 nm. However, continuously thickening SOT channels will directly increase the switching current in SOT-MRAM although the switching current density may decrease, which will thus increase the power consumption and is not favorable for the memory density because larger transistors should be used to provide larger writing currents.

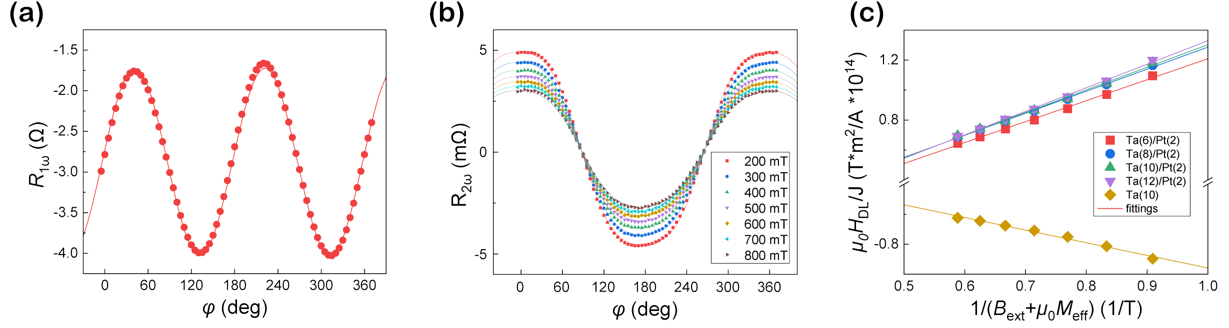

Figure B1 (a) First and (b) second harmonic Hall resistance of Ta(8)/Pt(2)/CoFeB(1.5). (c) Effective damping-like field generated by unit current density $\mu_0 H_{\rm DL}/J$ as a function of $(B_{\rm ext} + \mu_0 M_{\rm eff})^{-1}$ for different samples.

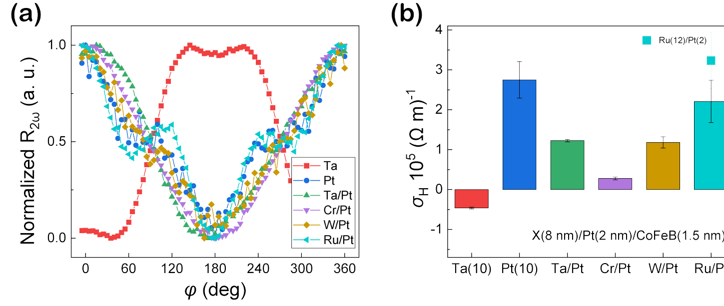

Figure C1 (a) Normalized second harmonic Hall voltages and (b) $\sigma_{\rm H}$ for samples with Ta(10), Pt(10), X(8)/Pt(2) (X = Ta, Cr, W, Ru) SOT channels.

Appendix D Current-induced magnetization switching of Ta/Pt samples

We further investigated the SOT-induced perpendicular magnetization switching in Ta(8-12)/Pt(2)/Co(0.65). We are interested in the system with PMA because inserting the converter Pt could result in an increase of the Gilbert damping constant α in the FM layer, but the critical switching current density $J_{\rm c}$ is proportional to α for the in-plane magnetized counterpart. Differently, the $J_{\rm c}$ barely increases with α for the PMA system, especially when the field-like torque is negligible [5]. In addition, it has been shown that the Pt-based HFL SOT scheme could withstand 400°C post-annealing and ensure enough thermal stability for devices down to 20 nm [6, 7]. Therefore, we selected the 0.65 nm Co as the FM layer to explore the switching performance.

The stack was initially annealed at 300°C for 20 minutes in the absence of the magnetic field. Figure D1(a) shows the AHE resistance for devices with different $t_{\rm Ta}$. The sharp hysteresis loop while sweeping the magnetic field at z direction and coercivity field larger than 18 mT indicate well-formatted PMA in our samples. The perpendicular anisotropy field $\mu_0 H_{\rm K}$ was validated to be ~ 0.25 T by fitting the $R_{\rm AHE} - H_{\rm x}$ curves around zero field using $R_{\rm AHE} \propto \sqrt{1-(H_{\rm x}/H_{\rm K})^2}$ as shown in Figure D1(b). To measure the current-induced magnetization switching, we injected SOT write current pulses of varying magnitudes and 10 ms width in x direction, followed by the reading pulse to detect the magnetization state through monitoring the AHE resistance.

Figure D1(c) shows the typical switching curve for the devices with $t_{\rm Ta} = 11.7$ nm. An in-plane magnetic field $\mu_0 H_{\rm x}$ of ± 48 mT was applied for deterministic SOT switching. Upon reversing the direction of $H_{\rm x}$, the switching polarity is also reversed, consistent with the feature of SOT switching in the PMA system [8]. We observe current-induced magnetic switching in all devices varying Ta thickness from 8 nm to 12 nm as depicted in Figure D1(d). Figure 1(f) summarizes the critical switching current density $J_{\rm c}$, which was taken when the AHE resistance was changed by 50%. Note that the $J_{\rm c}$ is calculated by the applied current in X/Pt layers divided by the product of the thickness of X/Pt bilayers and the actual width of the fabricated Hall-bar, and the current injected in FM layers was excluded. The $J_{\rm c}$ generally decreases with the thickness of Ta. The slightly increased $J_{\rm c}$, when $t_{\rm Ta}$ is around 8-9 nm, may be caused by the inhomogeneous fabrication process or random switching current distributions among Hall-bar devices. A series of $J_{\rm c}$ that much lower than the $J_{\rm c}$ of Pt/Co bilayer is obtained. Although the $J_{\rm c}$ may increase in the HFL structure due to the increased thickness of FM layers, it can be further improved by engineering the interlayer coupling energy and the parameters of the FM layers.

Appendix E Confirmation of the contribution of OHE in Ta/Pt bilayer

As a newly observed path to efficiently switch magnetic moments, orbital current, generated by OHE and OREE, has attracted massive interests. Due to the same electrical measurements to characterize the SOT, one needs to be cautious to distinguish OHE from SHE for clarifying its presence. In our experiments, if we assume that the spin currents generated by the X layer totally decay in the converter Pt and neglect any orbital effects, then the measured SOT may be attributed to the SHE in Pt only. Among the above data analysis, we treat the X/Pt bilayer as a hybrid SOT channel and the $J_{\rm SOT}$ is the average current density flowing in the channel. However, the current density in the Pt layer $J_{\rm SOT,Pt}$ could be much higher than $J_{\rm SOT}$ if the orbital source X has a larger resistivity than that of the converter. As such, the calculated charge-to-spin conversion efficiency $\theta_{\rm H,Pt}$ could be lower than the above $\theta_{\rm H}$, as indicated by our derivation in Eq. (3):

$$\frac{\theta_{\rm H,Pt}}{\theta_{\rm H}} = \frac{\frac{\rho_{\rm Pt}}{\rho_{\rm X}} t_{\rm X} + t_{\rm Pt}}{t_{\rm X} + t_{\rm Pt}}, \tag{E1}$$

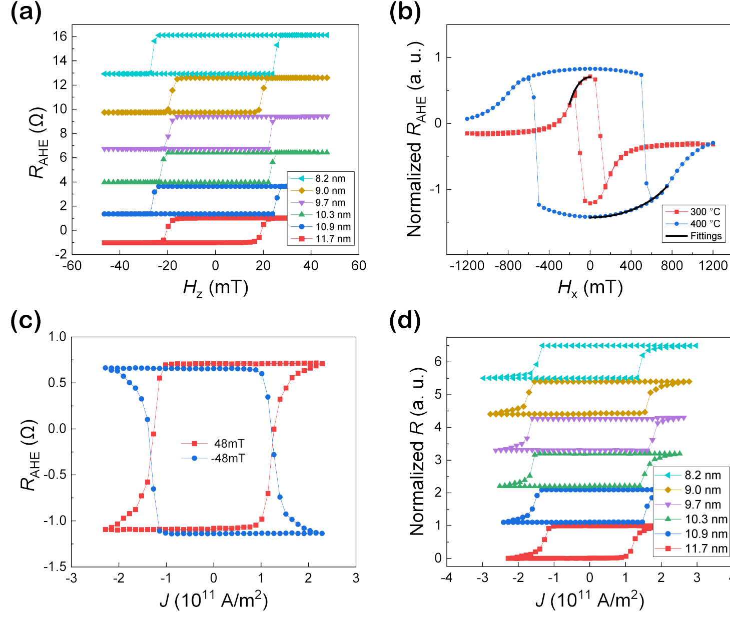

Figure D1 (a) H_z dependent AHE resistance signal in devices with different thicknesses of Ta layer. (b) H_x dependent AHE resistance signal with $t_{Ta} = 11.7$ nm after annealing at 300°C or 400°C. The anisotropy field $\mu_0 H_K$ can be evaluated by fitting the R_{AHE} - H_x curves around zero field. (c) Current-induced magnetization switching in a Hall bar device with $t_{Ta} = 11.7$ nm. An external in-plane magnetic field $H_x = \pm 48$ mT is applied. (d) Current-induced magnetization switching in devices with different thicknesses of Ta layer, an external in-plane magnetic field $H_x = +48$ mT is applied.

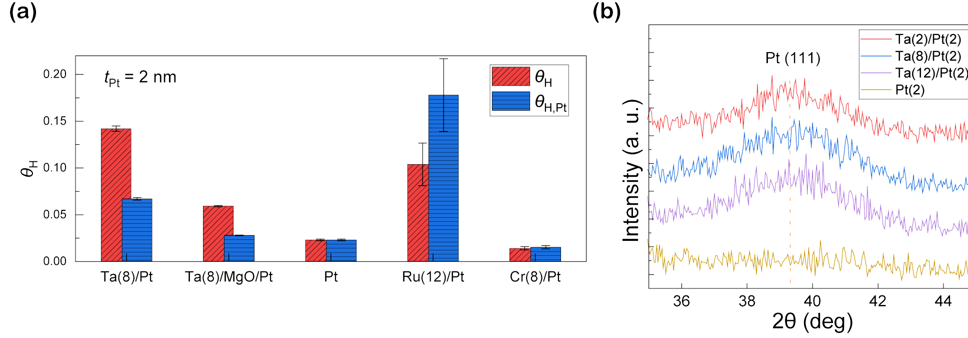

Figure E1 (a) Exclusion of SHE in Pt as the only spin current source in the X/Pt bilayers. Experimentally measured θ_H and calculated $\theta_{H,Pt}$ are denoted as red and blue histograms, respectively. All the samples shown in this figure have a Pt layer of 2 nm. (b) XRD analysis of Ta/Pt samples.

where $\rho_{Pt} = 55$ $\mu\Omega$·cm is the resistivity of Pt, $\rho_X = 162$ $\mu\Omega$·cm for X = Ta. t_X and t_{Pt} are the thicknesses of the X or Pt layer, respectively. Using Eq. (3), the $\theta_{H,Pt}$ for the Ta(8)/Pt(2) sample is calculated as 0.067 (Figure E1(a)), which looks somewhat reasonable. To further verify the effect of OHE, we further prepared a control sample, namely, Ta(8)/MgO(5)/Pt(2)/CoFeB(1.5)/MgO(1.5)/Ta(2), which is referred to as Ta(8)/MgO/Pt for simplicity. The insertion layer of 5 nm MgO is believed to hinder the orbital current from entering the Pt layer. As shown in Figure E1(a), the θ_H for the Ta(8)/MgO/Pt is much lower and is close to the value of Pt(2), indicating that the SHE in Pt is not the only spin current source.

Eq. (3) also reveals that the calculated $\theta_{H,Pt}$ could be much higher than the above θ_H if $\rho_{Pt} > \rho_X$. We prepared another series of samples with X being Ru because $\rho_{Ru} = 30$ $\mu\Omega$·cm: Ru(t_{Ru})/Pt(2)/ CoFeB(1.5)/MgO(1.5)/Ta(2). The calculated $\theta_{H,Pt}$ for $t_{Ru} = 12$ nm reaches 0.178 (Figure E1(a)), which is unrealistically high for a Pt layer of only 2 nm. We also analyzed the $\theta_{H,Pt}$ for the Cr(8)/Pt(2) sample with $\rho_{Cr} = 50$ $\mu\Omega$·cm, i.e., close to ρ_{Pt}. The calculated $\theta_{H,Pt}$ is approximately equal to θ_H, and is close to the value of Pt(2), which not only indicates the low OHE efficiency in Cr(8) layer, but also shows the evidence of OHE in Ta or Ru layers. All the evidences exclude SHE in Pt as the only spin current source. The different behavior when $X = \mathrm{Ta}, \mathrm{Ru}$ or Cr suggests the requirement of careful analysis of the SOT data in X/Pt bilayers.

These control experiments, together with the energy-efficient magnetization switching in Figure 1(f), unambiguously demonstrate the existence of OHE in Ta/Pt and Ru/Pt bilayer. Further, the resistivity measurements in Appendix A indicate that Ta layers prepared by condition 1 reach the stable β phase in our samples, excluding the impact on the θ_H may be induced by the crystallization difference of Ta layer. Through our X-ray diffraction (XRD) measurements (Figure E1(b)), we can exclude the impact of the different crystallization of Pt layers since the θ_H is increasing with Ta thickness while the Pt(111) peak remains nearly the same. In contrast, our experiments can be well interpreted by the incorporation of the OHE. As predicted theoretically, Ta and Ru possess positive orbital Hall conductivity (OHC) of $\sim 4.1 \times 10^5$ $(\frac{\hbar}{e} \cdot \Omega^{-1} \cdot \mathrm{m}^{-1})$ and $\sim 9 \times 10^5$ $(\frac{\hbar}{e} \cdot \Omega^{-1} \cdot \mathrm{m}^{-1})$, respectively [9]. Since Pt possesses positive SOC, the converted spin current has the same sign as the orbital current injected in the Pt layer, thus enhancing the effective θ_H. On this basis, the θ_H in Ta(8)/Pt(10), which is lower than that of Ta(8)/Pt(3), can also be well understood because

less current flows through the Ta layer, generating less orbital current, or orbital current generated in Ta layer is strongly scattered in Pt(10) layer.

References

1 Avci C O, Garello K, Gabureac M, et al. Interplay of spin-orbit torque and thermoelectric effects in ferromagnet/normal-metal bilayers. Phys Rev B, 2014, 90: 224427.
2 Hayashi M, Kim J, Yamanouchi M, et al. Quantitative characterization of the spin-orbit torque using harmonic Hall voltage measurements. Phys Rev B, 2014, 89: 144425.
3 Lee S, Kang M-G, Go D, et al. Efficient conversion of orbital Hall current to spin current for spin-orbit torque switching. Commun Phys, 2021, 4: 234.
4 Hayashi H, Jo D, Go D, et al. Observation of long-range orbital transport and giant orbital torque. Commun Phys, 2023, 6: 32.
5 Zhu D, and Zhao W. Threshold Current Density for Perpendicular Magnetization Switching through Spin-Orbit Torque. Phys Rev Appl, 2020, 13: 044078.
6 Couet S, Rao S, van Beek S, et al. BEOL compatible high retention perpendicular SOT-MRAM device for SRAM replacement and machine learning, IEEE Symposium on VLSI Technology, 2021, 1–2.
7 Van Beek S, Cai K, Yasin F, et al. Scaling the SOT track – A path towards maximizing efficiency in SOT-MRAM, International Electron Devices Meeting (IEDM), 2023, 1–4.
8 Peng S, Zhu D, Li W, et al. Exchange bias switching in an antiferromagnet/ferromagnet bilayer driven by spin–orbit torque. Nat Electron, 2020, 3: 757–764.
9 Salemi L, and Oppeneer P M. First-principles theory of intrinsic spin and orbital Hall and Nernst effects in metallic monoatomic crystals. Phys Rev Mater, 2022, 6: 095001.